


Cosmological probes of helium reionization

Selim C. Hotinli^{*}

*William H. Miller III Department of Physics and Astronomy, Johns Hopkins University,
3400 North Charles Street, Baltimore, Maryland 21218, USA*

 (Received 20 March 2023; accepted 1 August 2023; published 23 August 2023)

Joint analysis of cosmic microwave background (CMB) and large-scale structure at high redshifts provide new and unique windows into unexplored epochs of early structure formation. Here, we demonstrate how cosmic infrared background and high-redshift galaxies can be jointly analyzed with CMB to probe the epoch of helium reionization ($2 < z < 4$) on the light cone using kinetic Sunyaev Zel'dovich tomography. Characterizing this epoch has great potential significance for understanding astrophysics of galaxy formation, quasar activity and formation of the supermassive black holes. We find a detection at $8\text{--}10\sigma$ can be expected from combinations of data from CCAT prime, Vera Rubin Observatory, and CMB-S4 in the upcoming years.

DOI: [10.1103/PhysRevD.108.043528](https://doi.org/10.1103/PhysRevD.108.043528)

I. INTRODUCTION

The epoch of large-scale ionization of the second electron in helium (hereafter “helium reionization”) carries a large amount of information about astrophysics and cosmology. Recently Ref. [1] showed that the joint analysis of cosmic microwave background (CMB) and high-redshift ($2 < z < 4$) galaxy number-density fluctuations can be used to probe helium reionization via the technique of kinetic Sunyaev-Zel'dovich (kSZ) tomography (i.e. velocity reconstruction) (e.g. [2–14]) and found a high-significance detection at $\sim 10\sigma$ can be expected from Vera Rubin Observatory (LSST) [15] and CMB-S4 [16,17] surveys in the near future. Here, we extend the calculations performed in Ref. [1] to the more physically motivated light-cone formalism and consider new and more complete set of large-scale structure (LSS) tracers, including the cosmic infrared background (CIB), high-redshift quasars and weak gravitational lensing of the CMB.

The detection of helium reionization proposed here relies on the increase in the electron fraction that results from ionizing helium. Since helium accounts for 8% of the baryonic nuclei by number (25% by mass), the number of electrons increases by an extra 8% compared to protons in the first reionization of helium (which occurs together with the hydrogen reionization), and then another 8% in the second reionization. Unlike reionization of hydrogen or the first reionization of helium, astrophysical models indicate photons emitted by the first stars are not sufficiently energetic to fully ionize the second electron in helium

throughout the Universe. The reionization of helium thus requires the emergence of large numbers of quasars or active galactic nuclei (AGN) therefore occurs later and depends strongly on the properties of quasars and AGN, such as their accretion mechanisms [18], luminosity function [19–23], variability and lifetimes [24,25], as well as the growth and evolution of supermassive black holes [26].

Probing helium reionization can also have implications for cosmology as the total change in the free-electron fraction during this time is a measure of the primordial helium abundance Y_p . Increasing the measurement accuracy on Y_p may improve our understanding of the big bang nucleosynthesis, weak interaction rates, neutron lifetime (see e.g. for a review [27]), as well as breaking the degeneracy between Y_p and the number or relativistic degrees of freedom N_{eff} [28]; potentially providing valuable insights into our cosmological history.

The precise details of helium reionization, such as its duration, timing and morphology, are largely unknown. While surveys of helium and hydrogen Ly α forest can provide some evidence for the details of this epoch, these measurements—although likely more accurate in principle than the methods we discuss in this paper—are difficult in practice and are subject to severe astrophysical and systematic uncertainties about the inferred flux levels of the Ly α forest [29–32]. Surveys of helium Ly α , for example, are subject to intervening Lyman-limit systems at lower redshift [32], significantly reducing the prospects of characterizing the epoch of helium reionization unambiguously from these observables. Hydrogen Ly α , on the other hand, provides only an indirect evidence for helium reionization through probing the thermal history of inter-galactic medium (IGM), whose measurements are subject to significant systematic and modeling uncertainties [29–31].

^{*}shotinl1@jhu.edu

These suggest additional probes of helium reionization we consider here will be valuable for increasing the prospects to unambiguously characterizing this epoch.

This paper is organized as follows: In Sec. II we introduce various high-redshift probes of large-scale structure such as the kSZ effect, CIB, weak-lensing of the CMB and high-redshift galaxies. In Sec. III we describe the method of kSZ tomography using galaxies and CIB as tracers of the small-scale electron distribution. We describe our choices to model upcoming CMB and LSS experiments and demonstrate the prospects of detecting velocities using CIB in Sec. IV. We assess the prospects to detect and characterize helium reionization from these probes using kSZ tomography in Sec. V. We conclude with a discussion of the path to probing helium reionization with joint analysis of CMB and LSS in Sec. VI.

II. COSMOLOGICAL PROBES OF COSMIC (FORE)NOON

A. The kSZ effect

The temperature perturbation sourced due to the kSZ effect along the line of sight $\hat{\mathbf{n}}$ takes the form

$$T(\hat{\mathbf{n}})|_{\text{kSZ}} = -\sigma_T \int d\chi a n_e(\chi \hat{\mathbf{n}}) v_r(\chi \hat{\mathbf{n}}), \quad (1)$$

where σ_T is the Thomson scattering cross section, a is the scale factor, χ is the comoving distance, $n_e(\chi \hat{\mathbf{n}})$ is the free electron density along the line of sight, and $v_r(\chi \hat{\mathbf{n}})$ is the remote dipole field at the electrons' rest frame, which we approximate to be equal to the peculiar radial velocity of electrons throughout this paper.¹ The free electron density is proportional to $\bar{x}_e(z)$, the spatially averaged free electron fraction, which we define as the ratio of free electrons per hydrogen atom, which varies from zero to unity during reionization of hydrogen. The ionization of each electron in helium increases the ionization fraction by another ~ 8 percent, set by the primordial helium abundance.

B. The CIB signal

The CIB signal is sourced by the thermal radiation of dust grains in distant star-forming galaxies. Dust grains absorb the ultraviolet starlight, heat up and reemit light in the infrared. As star formation rate (SFR) of our Universe peak at around $z \sim 2-3$, the CIB is sourced dominantly from galaxies at around these redshifts, coinciding with the epoch of helium reionization. Currently available CIB maps provided by *Planck* [34] already allow CIB power spectrum to be measured up to around subdegree scales, sufficient for cosmological and astrophysical inference

¹In reality, Sachs-Wolfe effects also contribute to the remote dipole observed at the electrons' rest frame which can lead to a $\sim 5-10\%$ effect on the angular power-spectrum of the remote dipole field on large scales and early redshifts [2,11,33].

(see e.g. Refs. [35–38]), while upcoming measurements of CCAT-Prime will allow high-resolution measurements of CIB down to arc-minute scales [39].

The CIB brightness $I_\nu(\hat{\mathbf{n}})$ at frequency ν is given by the line-of-sight integral

$$I_\nu(\hat{\mathbf{n}}) = \int_0^{\chi_s} d\chi a(\chi) j_\nu(\chi \hat{\mathbf{n}}), \quad (2)$$

where $j_\nu(\chi \hat{\mathbf{n}})$ is the emissivity density fluctuations which we write as $j_\nu(\chi \hat{\mathbf{n}}) = \bar{j}_\nu(\chi)[1 + \delta_{j_\nu}(\chi \hat{\mathbf{n}})]$, where $\delta_{j_\nu}(\chi \hat{\mathbf{n}})$ is the emissivity overdensity and $\bar{j}_\nu(\chi)$ is the mean emissivity density defined as an integral over the luminosity density

$$\bar{j}_{\nu_{\text{em}}}(\chi) = \int dL_{\nu_{\text{em}}} \frac{dN}{dL_{\nu_{\text{em}}}} \frac{L_{\nu_{\text{em}}}}{4\pi}, \quad (3)$$

where $\nu_{\text{em}} = (1+z)\nu$ is the frequency corresponding to the redshift of the emitted radiation and dN/dL_ν is the luminosity function defined such that $dL_\nu(dN/dN_\nu)$ gives the number density of galaxies within luminosity between L_ν and $L_\nu + dL_\nu$. We model the CIB autospectra as

$$C_\ell^{I_\nu I_\nu, \text{obs}} = C_\ell^{I_\nu I_\nu} + N_\ell^{\nu, \text{SN}} + N_\ell^{\nu, I_\nu}, \quad (4)$$

where $C_\ell^{I_\nu I_\nu}$ is the CIB signal, $N_\ell^{\nu, \text{SN}}$ is the shot noise term due to the finite number count of the galaxies sourcing the CIB signal and N_ℓ^{ν, I_ν} is the instrumental noise of the CIB measurement to be defined in Sec. IV. The CIB signal satisfies

$$C_\ell^{I_\nu I_\nu} = \int \frac{2}{\pi} \int d\chi d\chi' \int k^2 dk \times a(\chi) a(\chi') \bar{j}_\nu(\chi) \bar{j}_\nu(\chi') P_{jj}^{\nu\nu'}(k, \chi, \chi') j_\ell(k\chi) j_\ell(k\chi'), \quad (5)$$

where $j_\ell(k\chi)$ is the spherical Bessel function and $(2\pi)^3 \delta^3(\mathbf{k} - \mathbf{k}') P_{\delta_j \delta_j}^{\nu\nu'}(k, \chi, \chi') = \langle \delta_{j_\nu}(\mathbf{k}, \chi') \delta_{j_\nu}(\mathbf{k}', \chi') \rangle$ is the power-spectrum of the emissivity overdensity.

We calculate the power-spectrum of the emissivity overdensity using the halo model, setting

$$P_{\delta_j \delta_j}^{\nu\nu'}(k, \chi, \chi') = P_{\delta_j \delta_j}^{\nu\nu', 1h}(k, \chi, \chi') + P_{\delta_j \delta_j}^{\nu\nu', 2h}(k, \chi, \chi'). \quad (6)$$

Here, the 2-halo term $P_{jj}^{\nu\nu', 2h}(k, \chi, \chi')$ satisfies

$$\bar{j}_\nu(\chi) \bar{j}_\nu(\chi') P_{\delta_j \delta_j}^{\nu\nu', 2h}(k, \chi) = D_\nu(\chi) D_{\nu'}(\chi') P_{\text{lin}}(k, z), \quad (7)$$

where

$$D_\nu(\chi) = \frac{1}{4\pi} \int dM \frac{dN}{dM} b_h(M, \chi) [L_{\nu_{\text{em}}}^{\text{cen}} + L_{\nu_{\text{em}}}^{\text{sat}} u(k, M, \chi)]$$

is the CIB bias, $b_h(M, \chi)$ is the halo bias, dN/dM is the halo mass function, $P_{\text{lin}}(k, z)$ is the linear matter-density power spectrum and $u(k, M, z)$ is the (normalized) Fourier transform of the halo density profile. Here $L_{\nu_{\text{em}}}^{\text{cen}}(M, z)$ and $L_{\nu_{\text{em}}}^{\text{sat}}(M, z)$ are the central and satellite galaxy luminosities, respectively, and we omit showing their mass and redshift dependencies in notation for brevity. The 1-halo term can be calculated as

$$\begin{aligned} \bar{j}_\nu(\chi) \bar{j}_{\nu'}(\chi') P_{\delta_j \delta_j}^{\nu \nu' 1h}(k, \chi) &= \int dM \frac{dN}{dM} \frac{1}{(4\pi)^2} \\ &\times \left[L_{\nu_{\text{em}}}^{\text{cen}} L_{\nu'_{\text{em}}}^{\text{sat}} u(k, M, \chi) \right. \\ &+ L_{\nu'_{\text{em}}}^{\text{cen}} L_{\nu_{\text{em}}}^{\text{sat}} u(k, M, \chi) \\ &\left. + L_{\nu_{\text{em}}}^{\text{sat}} L_{\nu'_{\text{em}}}^{\text{sat}} |u(k, M, \chi)|^2 \right], \quad (8) \end{aligned}$$

where the central-galaxy luminosity function $L_{\nu_{\text{em}}}^{\text{cen}}$ satisfies

$$L_{\nu_{\text{em}}}^{\text{cen}} = N^{\text{cen}}(M, z) L_{\nu_{\text{em}}}^{\text{gal}}(M, z). \quad (9)$$

Here, $N^{\text{cen}}(M, z)$ is the number of central galaxies in a halo of mass M at redshift z , and $L_{\nu_{\text{em}}}^{\text{gal}}(M, z)$ is the luminosity function of the host galaxy. The satellite galaxy luminosity function $L_{\nu_{\text{em}}}^{\text{sat}}$ is given by

$$L_{\nu_{\text{em}}}^{\text{sat}}(M, z) = \int dM_s \frac{dN}{dM_s} L_{\nu_{\text{em}}}^{\text{gal}}(M_s, z), \quad (10)$$

where $N^{\text{sat}} = \int dM_s (dN/dM_s)$ and dN/dM_s is subhalo mass function. Finally, the CIB shot noise can be written as

$$N_{\ell}^{\nu, \text{NS}} = \int dS_\nu \frac{dN}{dS_\nu} S_\nu^2, \quad (11)$$

where S_ν is the flux measured at frequency ν . Our calculation of the CIB spectra follows Refs. [40,41] and the halo model described in Ref. [3]. Throughout this paper we use the `ReCCO`² code (described in detail in Ref. [42]) when calculating observables.

We show the CIB signal at various frequencies with blue solid curves on the left panel of Fig. 2. There, the solid purple lines correspond to the total observed CIB signal including the shot noise and the detector noise. The dashed blue curves correspond to shot noise and the dotted purple curves correspond to detector noise. The solid gray and red lines correspond to CMB spectrum anticipated to be observed by Simons observatory and CMB-S4, respectively. We describe the experimental configurations used for noise contributions to these plots in Sec. IV.

²Publicly available at <https://github.com/jcayuso/ReCCO>.

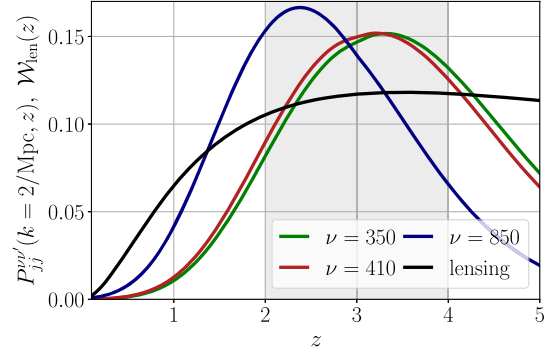


FIG. 1. Redshift dependence of the anticipated CIB brightness power spectra $\nu^2 (2\pi)^3 \delta(\mathbf{k} - \mathbf{k}') P_{jj}^{\nu \nu'}(k, z) = \langle j_\nu(\mathbf{k}) j_{\nu'}(\mathbf{k}') \rangle$ at wave number $k = 2 \text{ Mpc}^{-1}$, shown together with the redshift kernel of weak gravitational lensing $\mathcal{W}_{\text{len}}(z) \propto \chi(1 - \chi/\chi_*)$. All curves are normalized to unity once integrated within the redshift range $z \in [0.1, 5.0]$. The light-gray-shaded region corresponds to the redshift range anticipated to correspond to the epoch of helium reionization, $2 \lesssim z \lesssim 4$, where these signals can be seen to get significant contribution. Lines labeled as $\nu = \{350, 410, 850\}$ correspond to the anticipated observation frequencies of the upcoming CCAT-Prime survey.

C. Weak gravitational lensing of the CMB

The CMB lensing potential is defined as

$$\phi(\hat{\mathbf{n}}) \equiv -2 \int_0^{\chi_*} d\chi \frac{\chi^* - \chi}{\chi \chi^*} \Phi(\chi \hat{\mathbf{n}}), \quad (12)$$

where $\Phi(\chi \hat{\mathbf{n}})$ is the gravitational potential. The gravitational interaction of CMB photons and the large-scale structure intervening between the recombination surface and detectors on Earth deflects CMB photons by an angle given by $\boldsymbol{\alpha} = \nabla \phi$. We show the anticipated lensing (deflection) power spectrum $C_{\ell}^{\phi\phi} = \ell(\ell + 1) C_{\ell}^{\phi\phi}$ on the right panel of Fig. 2, along with the lensing-reconstruction noise calculated using the standard lensing quadratic estimator following [43]. Here, we used the `CLASS_DELENS`³ code to calculate the lensing reconstruction noise, assuming experimental configurations matching the Simons Observatory and CMB-S4, which are described below. The redshift dependence of the lensing signal $\mathcal{W}_{\text{len}}(z) \propto \chi(1 - \chi/\chi^*)$ was shown in Fig. 1, suggesting lensing gets significant contribution from high redshifts corresponding to the epoch of helium reionization. The cross power of lensing deflection with the radial velocity and galaxy fluctuations are given in Ref. [42].

D. Galaxies

Similar to the bin-averaged radial-velocity and optical-depth fields, we construct a two-dimensional galaxy density field as an integral over a given redshift bin as

³Publicly available at https://github.com/selimhotinli/class_delens.

$$\delta_g^\alpha(\hat{\mathbf{n}}) = \int_{\chi_\alpha^{\min}}^{\chi_\alpha^{\max}} d\chi_\alpha \mathcal{W}_{\text{gal}}(\chi_\alpha) \delta_g(\chi_\alpha \hat{\mathbf{n}}), \quad (13)$$

where

$$\mathcal{W}_{\text{gal}}(\chi_\alpha) = H(z_\alpha) \int d\chi W(\chi) P(z_\alpha, z(\chi)) \quad (14)$$

is the effective window function taking into account the photo- z errors, and

$$P(z, z_\alpha) = \bar{P}(z) \exp\left[-\frac{(z_\alpha - z)^2}{2\sigma_z}\right], \quad (15)$$

with $\bar{P}(z) = \int_0^\infty dz' \exp[-(z' - z)^2/2\sigma_z]$. Here, σ_z is the anticipated photo- z error for a given galaxy survey.

The observed angular power spectrum between redshift-binned galaxy density fluctuations from a photometric survey can then be expressed as

$$\begin{aligned} C_{\ell, \alpha\beta}^{\delta_g \delta_g, \text{obs}} &= 16\pi^2 \int_{\chi_\alpha^{\min}}^{\chi_\alpha^{\max}} d\chi_\alpha \int_{\chi_\beta^{\min}}^{\chi_\beta^{\max}} d\chi_\beta \mathcal{W}_{\text{gal}}(\chi_\alpha) \mathcal{W}_{\text{gal}}(\chi_\beta) \\ &\times \int \frac{dk k^2}{(2\pi)^3} j_\ell(k\chi_\alpha) j_{\ell'}(k\chi_\beta) P_{gg}(\chi_\alpha, \chi_\beta, k) \\ &+ \delta_{\alpha\beta} \frac{1}{n_g(z_\alpha)}, \end{aligned} \quad (16)$$

where $P_{gg}(\chi_\alpha, \chi_\beta, k)$ is the galaxy-galaxy power spectrum which we compute using the halo model as prescribed in Ref. [42]. Here, $n_{\text{gal}}(z_\alpha)$ is the galaxy shot noise which we define in Sec. IV. The cross power of the galaxy and radial velocity fluctuations on large scales is defined in Ref. [42].

III. VELOCITY RECONSTRUCTION

A. kSZ tomography

An important consequence of the kSZ effect is that the cross power of the CMB and a tracer of electron fluctuations (such as the distributions of galaxies or the CIB signal) becomes anisotropic on small scales; varying over the sky in a way dependent on the fluctuations of the bulk radial velocities of electrons. The cross correlation of the kSZ effect and a tracer of density fluctuations such as the galaxy overdensity $\delta_g^\beta(\chi \hat{\mathbf{n}})$ inside some redshift bin β can be written on the curved sky in terms of spherical harmonic coefficients as

$$\begin{aligned} \langle T_{\ell m} \delta_{\ell' m'}^\beta \rangle &= \sum_\alpha \sum_{L M L' M'} \bar{v}_{L' M'}^\alpha \langle \tau_{LM}^\alpha \delta_{g, L' M'}^\beta \rangle \\ &\times \int d^2 \hat{\mathbf{n}} Y_{\ell m}^*(\hat{\mathbf{n}}) Y_{LM}(\hat{\mathbf{n}}) Y_{L' M'}(\hat{\mathbf{n}}), \end{aligned} \quad (17)$$

where $\langle \tau_{\ell m}^\alpha \delta_{\ell' m'}^{\beta} \rangle \equiv C_{\ell \ell'}^{\tau_\alpha \delta_\beta} \delta_{\ell \ell'} \delta_{m m'}$. Here \bar{v}_{LM}^α is the spherical-harmonic transform of the mean radial velocity field averaged over a redshift bin. The radial-velocity field at the comoving distance χ_α can also be parametrized as $v_r(\chi \hat{\mathbf{n}}) = \bar{v}_r^\alpha(\hat{\mathbf{n}})[1 + \delta v_r(\chi \hat{\mathbf{n}})]$ where \bar{v}_r^α radial-velocity field averaged within the comoving distance range $[\chi_\alpha^{\min}, \chi_\alpha^{\max}]$ and satisfy

$$\bar{v}_r^\alpha(\hat{\mathbf{n}}) = \frac{1}{\Delta\chi_\alpha} \int_{\chi_\alpha^{\min}}^{\chi_\alpha^{\max}} d\chi_\alpha v_r(\chi_\alpha \hat{\mathbf{n}}), \quad (18)$$

and $\bar{v}_{LM}^\alpha \equiv \int d\hat{\mathbf{n}} \bar{v}_r^\alpha(\hat{\mathbf{n}}) Y_{LM}(\hat{\mathbf{n}})$. We can similarly write the electron density field as $n_e(\chi \hat{\mathbf{n}}) = \bar{n}_e(\chi)[1 + \delta_e(\chi \hat{\mathbf{n}})]$ where $\bar{n}_e(\chi)$ is the sky-averaged electron density at the comoving distance χ and $\delta_e(\chi \hat{\mathbf{n}})$ is the fluctuations of electron overdensity. The anisotropies in the bin-averaged optical depth then satisfy

$$\tau^\alpha(\hat{\mathbf{n}}) = -\sigma_T \int_{\chi_\alpha^{\min}}^{\chi_\alpha^{\max}} d\chi a \bar{n}_e(\chi) [1 + \delta_e(\chi \hat{\mathbf{n}})], \quad (19)$$

where $\tau_{LM}^\alpha \equiv \int d\hat{\mathbf{n}} \tau^\alpha(\hat{\mathbf{n}}) Y_{LM}(\hat{\mathbf{n}})$ in Eq. (30), and the mean-field contributions to the kSZ signal in the CMB take the form

$$T(\hat{\mathbf{n}})|_{\text{kSZ}} = \sum_\alpha \tau^\alpha(\hat{\mathbf{n}}) \bar{v}_r^\alpha(\hat{\mathbf{n}}). \quad (20)$$

Rewriting the second line of Eq. (17) using Wigner-3J symbols we get

$$\langle T_{\ell m} \delta_{\ell' m'}^\beta \rangle = \sum_{\alpha, L' M'} (-1)^{m_1 + m_2} \Gamma_{\ell \ell' L'}^{\alpha\beta} \begin{pmatrix} \ell & \ell' & L' \\ m & -m' & M' \end{pmatrix} \bar{v}_{L' M'}^\alpha, \quad (21)$$

where

$$\Gamma_{\ell \ell' L'}^{\alpha\beta} \equiv \sqrt{\frac{(2\ell + 1)(2\ell' + 1)(2L' + 1)}{4\pi}} \begin{pmatrix} \ell & \ell' & L' \\ 0 & 0 & 0 \end{pmatrix} C_{L'}^{\tau_\alpha \delta_\beta}. \quad (22)$$

The program of reconstructing the large-scale radial-velocity field from this statistical anisotropy is called ‘‘kSZ tomography’’ where the unbiased and minimum-variance quadratic estimator for the redshift-binned bulk velocity field takes the form

$$\hat{v}_{\ell m}^\alpha = A_\ell^\alpha (-1)^m \sum_{\ell' m' L M} \begin{pmatrix} \ell & \ell' & L \\ 0 & 0 & 0 \end{pmatrix} \Gamma_{\ell' L}^{\alpha\beta} \frac{T_{\ell' m'} \delta_{L M}^\beta}{C_{\ell'}^{TT} C_L^{\delta_g^\beta}}, \quad (23)$$

with the reconstruction noise of the estimator satisfying

$$N_{\alpha\ell}^{\bar{v}\bar{v},\text{kSZ}} = \left[\frac{1}{2\ell+1} \sum_{\ell'L} \frac{\Gamma_{\ell'L\ell}^{\alpha\beta} \Gamma_{\ell'L\ell}^{\alpha\beta}}{C_{\ell'}^{\text{TT,obs}} C_L^{\delta_g^{\beta},\text{obs}}} \right]^{-1}. \quad (24)$$

The nominator of the summed term inside the brackets in Eq. (24) contains a product of two Wigner-3J symbols which can be written as an integral of the product of three Wigner-d matrices using the equality

$$\begin{aligned} & \int_{-1}^1 d(\cos\theta) d_{s_1 s'_1}^{\ell_1}(\theta) d_{s_2 s'_2}^{\ell_2}(\theta) d_{s_3 s'_3}^{\ell_3}(\theta) \\ &= 2 \begin{pmatrix} \ell_1 & \ell_2 & \ell_3 \\ s_1 & s_2 & s_3 \end{pmatrix} \begin{pmatrix} \ell_1 & \ell_2 & \ell_3 \\ s'_1 & s'_2 & s'_3 \end{pmatrix}, \end{aligned} \quad (25)$$

which gives

$$N_{\alpha\ell}^{\bar{v}\bar{v},\text{kSZ}} = 2\pi \int_{-1}^1 d(\cos\theta) \zeta_1(\theta) \zeta_2^{\alpha\beta}(\theta) d_{00}^{\ell}(\theta), \quad (26)$$

where

$$\zeta_1(\theta) = \sum_{\ell} \frac{(2\ell+1)}{4\pi} \frac{1}{C_{\ell}^{\text{TT,obs}}} \quad (27)$$

and

$$\zeta_2^{\alpha\beta}(\theta) = \sum_{\ell} \frac{(2\ell+1)}{4\pi} \frac{(C_{\ell}^{\tau\delta_g})^2}{C_{\ell}^{\delta_g, \text{obs}}}. \quad (28)$$

Here, the cross-correlation between the redshift-bin averaged optical depth and galaxy fields satisfy

$$\begin{aligned} C_{\ell, \alpha\beta}^{\tau\delta_g} &= 16\pi^2 \sigma_T \int_{\chi_a^{\min}}^{\chi_a^{\max}} d\chi_a \int_{\chi_b^{\min}}^{\chi_b^{\max}} d\chi_b a(\chi_a) \bar{n}_e(\chi_a) \mathcal{W}_{\text{gal}}(\chi_b) \\ &\times \int \frac{dkk^2}{(2\pi)^3} j_{\ell}(k\chi_a) j_{\ell}(k\chi_b) P_{eg}(\chi_a, \chi_b, k), \end{aligned} \quad (29)$$

where $P_{eg}(\chi_a, \chi_b, k)$ is the electron-galaxy cross power, determined by the model for the electron density profile inside dark matter halos, which depends on the physical processes such as AGN feedback. Throughout this paper we choose the ‘‘AGN’’ gas profile model from Ref. [44] to model electron profiles and use the ReCCO code for our calculations following Ref. [42].

B. Velocity reconstruction with the CIB

The cross-correlation of the kSZ effect and CIB intensity can be written as

$$\begin{aligned} \langle T_{\ell m} I_{\nu, \ell' m'} \rangle &= \sum_{\alpha} \sum_{LML'} \bar{v}_{L'M'}^{\alpha} \langle \tau_{LM}^{\alpha} I_{\nu, L'M'} \rangle \\ &\times \int d^2 \hat{\mathbf{n}} Y_{\ell m}^*(\hat{\mathbf{n}}) Y_{LM}(\hat{\mathbf{n}}) Y_{L'M'}(\hat{\mathbf{n}}), \end{aligned} \quad (30)$$

where $\langle \tau_{\ell m}^{\alpha} I_{\nu, \ell' m'} \rangle \equiv C_{\ell}^{\alpha I_{\nu}} \delta_{\ell \ell'} \delta_{mm'}$. Rewriting the second line of Eq. (30) with Wigner-3J symbols we get

$$\langle T_{\ell m} I_{\ell' m'} \rangle = \sum_{\alpha L'M'} (-1)^{m_1+m_2} \Gamma_{\ell \ell' L'}^{\alpha, \text{CIB}} \begin{pmatrix} \ell & \ell' & L' \\ m & -m' & M' \end{pmatrix} \bar{v}_{L'M'}^{\alpha}, \quad (31)$$

where

$$\Gamma_{\ell \ell' L'}^{\alpha, \text{CIB}} \equiv \sqrt{\frac{(2\ell+1)(2\ell'+1)(2L'+1)}{4\pi}} \begin{pmatrix} \ell & \ell' & L' \\ 0 & 0 & 0 \end{pmatrix} C_{L', \alpha}^{\tau I_{\nu}}. \quad (32)$$

Here, the cross-correlation between the bin-averaged optical depth and the CIB brightness can be written as

$$\begin{aligned} C_{\ell, \alpha}^{\tau I_{\nu}} &= 16\pi^2 \sigma_T \int_{\chi_a^{\min}}^{\chi_a^{\max}} d\chi_a \int_0^{\chi_*} d\chi_b j_{\ell}(k\chi_a) j_{\ell}(k\chi_b) \\ &\times a(\chi_a) \bar{n}_e(\chi_a) a(\chi_b) \bar{j}_{\nu}(\chi_b) \int \frac{dkk^2}{(2\pi)^3} P_{ej}^{\nu}(\chi_a, \chi_b, k), \end{aligned} \quad (33)$$

where $(2\pi)^3 \delta^3(\mathbf{k} - \mathbf{k}') P_{ej}^{\nu}(k, \chi, \chi') = \langle \delta_e(\mathbf{k}, \chi) \delta_j(\mathbf{k}', \chi') \rangle$ is the cross power between the fluctuations in CIB emissivity and electron density. Following Ref. [42], we calculate the 2-halo contribution to this cross power as

$$P_{XY}^{\nu, 2h}(k, z) = D_X(k, z) D_Y(k, z) P_{\text{lin}}(k, z), \quad (34)$$

where $P_{\text{lin}}(k, z)$ is the linear dark matter power spectrum and

$$D_X(k, z) = \int dM \frac{dN}{dM} b_h(M, z) A_X. \quad (35)$$

For the electron and emissivity fluctuations, these satisfy

$$A_e = \frac{M}{\rho_m} u_e(k, M, z) \quad (36)$$

and

$$A_j = \frac{1}{4\pi} [L_{v_{\text{cm}}}^{\text{cen}} + L_{v_{\text{cm}}}^{\text{sat}} u(k, M, \chi)], \quad (37)$$

where $u_e(k, M, z)$ is the electron density profile, which we set to the ‘‘AGN’’ gas profile defined in Ref. [44], and ρ_m is

the present day cosmological matter density. The 1-halo term for the cross-correlation can be calculated as

$$P_{ej}^{\nu,1h}(k, z) = \int dM \frac{dN}{dM} A_e(M, k, z) A_j(M, k, z). \quad (38)$$

Similar to the case of kSZ tomography with galaxies, we can now define a minimum-variance quadratic estimator for the bulk velocity field at some redshift bin α . Since both CMB and CIB are two-dimensional fields integrated along the line of sight, we first drop the constraint that the reconstructed redshift-binned velocity field must be unbiased. The *biased* minimum variance estimator can be written as

$$\hat{v}_{\ell m}^{(b)\alpha} = A_{\ell}^{\alpha}(-1)^m \sum_{\ell' m' L'} \begin{pmatrix} \ell & \ell' & L' \\ 0 & 0 & 0 \end{pmatrix} \Gamma_{\ell' L'}^{\alpha, \text{CIB}} \frac{T_{\ell' m'} I_{\nu, LM}}{C_{\ell'}^{TT} C_L^{I_{\nu} I_{\nu}}}, \quad (39)$$

where

$$A_{\ell}^{\alpha} = \left[\frac{1}{2\ell + 1} \sum_{\ell' L} \frac{\Gamma_{\ell' L}^{\alpha, \text{CIB}} \Gamma_{\ell' L}^{-\alpha, \text{CIB}}}{C_{\ell'}^{TT} C_L^{I_{\nu} I_{\nu}}} \right]^{-1}. \quad (40)$$

The velocity reconstruction noise then satisfies

$$N_{\ell, \alpha\beta}^{(b)\bar{v}\bar{v}} = \frac{A_{\ell}^{\alpha} A_{\ell}^{\beta}}{2\ell + 1} \sum_{\ell' L} \frac{\Gamma_{\ell' L}^{\alpha, \text{CIB}} \Gamma_{\ell' L}^{\beta, \text{CIB}}}{C_{\ell'}^{TT} C_L^{I_{\nu} I_{\nu}}}. \quad (41)$$

We can now define an *unbiased* quadratic estimator for the velocity as

$$\hat{v}_{\ell m}^{\alpha} = (R^{-1})_{\alpha\beta} \hat{v}_{\ell m}^{\beta}, \quad (42)$$

which satisfies $\langle \hat{v}_{\ell m}^{\alpha} \rangle = v_{\ell m}^{\alpha}$. The rotation matrix that debiases the reconstructed velocity can be found to satisfy

$$R_{\alpha\beta} = \left[\sum_{\ell' L} \frac{\Gamma_{\ell' L}^{\alpha, \text{CIB}} \Gamma_{\ell' L}^{-\alpha, \text{CIB}}}{C_{\ell'}^{TT} C_L^{I_{\nu} I_{\nu}}} \right]^{-1} \sum_{\ell' L} \frac{\Gamma_{\ell' L}^{\alpha, \text{CIB}} \Gamma_{\ell' L}^{\beta, \text{CIB}}}{C_{\ell'}^{TT} C_L^{I_{\nu} I_{\nu}}}. \quad (43)$$

The reconstruction noise for the unbiased minimum variance estimator satisfies

$$N_{\ell, \alpha\beta}^{\bar{v}\bar{v}} = (R^{-1})_{\alpha\gamma} (R^{-1})_{\beta\delta} N_{\ell, \gamma\delta}^{(b)\bar{v}\bar{v}} \delta_{\ell\ell'} \delta_{mm'}. \quad (44)$$

Finally, using the spherical-harmonic equality defined in Eq. (25), we rewrite the (biased) reconstruction noise as

$$N_{\ell, \alpha\beta}^{(b)\bar{v}\bar{v}} = 2\pi \frac{A_{\ell}^{\alpha} A_{\ell}^{\beta}}{2\ell + 1} \int_{-1}^1 d(\cos\theta) \zeta_1(\theta) \zeta_{2, \text{CIB}}^{\alpha\beta}(\theta) d_{00}^{\ell}(\theta), \quad (45)$$

where

$$\zeta_{2, \text{CIB}}^{\alpha\beta}(\theta) = \sum_{\ell} \frac{(2\ell + 1)}{4\pi} \frac{C_{\ell, \alpha}^{\tau I_{\nu}} C_{\ell, \beta}^{\tau I_{\nu}}}{C_{\ell}^{I_{\nu}, \text{obs}}} \quad (46)$$

and

$$A_{\ell}^{\alpha} = 2\pi \int_{-1}^1 d(\cos\theta) \zeta_1(\theta) \zeta_{2, \text{CIB}}^{\alpha\alpha}(\theta) d_{00}^{\ell}(\theta). \quad (47)$$

IV. FORECASTS

Throughout this paper we use the standard *Planck* cosmology with 6 Λ cold dark matter (Λ CDM) model parameters we define in Table I which we set equal to the fiducial parameters given there. The assumptions we make for the various observables we consider are defined in what follows.

A. CMB

We model the instrumental and atmospheric noise contributions to the CMB temperature as

$$N_{\ell}^{\text{TT}} = \Delta_T^2 \exp\left(\frac{\ell(\ell+1)\theta_{\text{FWHM}}^2}{8 \ln 2}\right) \left[1 + \left(\frac{\ell}{\ell_{\text{knee}}}\right)^{\alpha_{\text{knee}}} \right], \quad (48)$$

where Δ_T is the detector RMS noise and θ_{FWHM} is the Gaussian beam full width at half maximum. The second term inside the brackets in Eq. (48) corresponds to the ‘‘red’’ noise due to Earth’s atmosphere, parametrized by the terms ℓ_{knee} and α_{knee} . We define our choices for these parameters to match the ongoing and upcoming CMB surveys in Table II.

The millimeter-wavelength CMB signal gets contributions also from the black-body late-time and reionization kSZ, the Poisson and clustered CIB, as well as the thermal Sunyaev Zel’dovich (tSZ) effect foregrounds, which we calculate following Refs. [45,46]. We omit the cross-correlation between tSZ and CIB. We include radio sources following Ref. [47]. We calculate the lensed CMB black-body using CAMB [48].

B. Galaxy surveys

Galaxy surveys play a significant role in detecting velocity fluctuations upon cross correlation with

TABLE I. Fiducial cosmological parameters for the 6-parameter Λ CDM model we consider in our calculations throughout this paper.

Parameter	Fiducial value
Cold dark matter density ($\Omega_c h^2$)	0.1197
Baryon density ($\Omega_b h^2$)	0.0222
Angle subtended by acoustic scale (θ_s)	0.010409
Optical depth to recombination (τ)	0.060
Primordial scalar fluctuation amplitude (A_s)	2.196×10^{-9}
Primordial scalar fluctuation slope (n_s)	0.9655

TABLE II. Inputs to ILC noise: the beam and noise RMS parameters we assume for survey configurations roughly corresponding to the SO and CMB-S4. In all cases, we account for the degradation due to Earth’s atmosphere by defining the CMB noise choose $\ell_{\text{knee}} = 100$ and $\alpha_{\text{knee}} = -3$.

	Beam FWHM		Noise RMS μK	
	SO	CMB-S4	SO	CMB-S4
39 GHz	5.1'	5.1'	36	12.4
93 GHz	2.2'	2.2'	8	2.0
145 GHz	1.4'	1.4'	10	2.0
225 GHz	1.0'	1.0'	22	6.9
280 GHz	0.9'	0.9'	54	16.7

reconstructed radial-velocity fields from kSZ tomography. They also serve as small-scale tracers of the electron density and can be used for velocity reconstruction through cross correlation with CMB on small scales. As these programs will be pursued in the near future, we include in our analysis the galaxy density fields anticipated to be observed in the near future.

We consider the ongoing measurements of quasistellar objects with DESI [49] and high-redshift galaxies with photometric LSST survey [50]. We follow Ref. [49] for DESI quasars when calculating the number density and set the bias to satisfy $b_g(z) = 1.2/D(z)$. For LSST, we approximate the galaxy density of the “gold” sample, with $n_{\text{gal}}(z) = n_0[(z/z_0)^2 \exp(-z/z_0)/2z_0]$ with $n_0 = 40 \text{ arcmin}^{-2}$ and $z_0 = 0.3$ and take the galaxy bias as $b_g(z) = 0.95/D(z)$. For LSST, we consider the standard anticipated photo- z error $\sigma_z = 0.03(1+z)$ which becomes increasingly more detrimental at higher redshifts. For DESI, the photo- z errors will be small $\sigma_z \ll 1$. We show the galaxy bias and number density that we consider for these surveys for a range of redshifts in Table III for reference.

TABLE III. Assumed galaxy bias b_g and number density n_{gal} for DESI and LSST at various redshifts. We consider two choices for the expected distribution of quasistellar objects redshifts from DESI following Ref. [49] with two different quasar luminosity function r smaller than 22.5 and 23. For the LSST survey we take the anticipated number counts after 10 years of observations.

	$z = 1.9$	2.6	3.45	4.45	
LSST					
b_g	1.81	2.47	3.28	4.23	
$n_{\text{gal}} (\times 10^4) [\text{Mpc}^{-3}]$	14.9	2.9	0.34	0.02	Y10
DESI					
b_g	1.92	3.18	4.71	6.51	
$n_{\text{gal}} (\times 10^6) [\text{Mpc}^{-3}]$	1.61	0.80	0.15	0.03	$r < 22.5$
$n_{\text{gal}} (\times 10^6) [\text{Mpc}^{-3}]$	2.20	1.18	0.30	0.04	$r < 23.0$

TABLE IV. Inputs to instrumental noise parameters defined in Eq. (49) matching the specifications of *Planck* and the upcoming CCAT-Prime. We account for the “red” noise due to Earth’s atmosphere on the latter measurement by setting $\ell_{\text{knee}} = 100$, $\alpha_{\text{knee}} = -3.5$ and $\Delta_R^2 = 1000$.

Frequencies (GHz)	<i>Planck</i>			CCAT-Prime		
	353	545	857	350	410	850
θ_{FWHM}	4.94'	4.83'	4.64'	37''	32''	15''
$\Delta_T (\mu\text{K} - \text{arcmin})$	0.036	0.20	4.85	107	407	6.8×10^5

C. The CIB noise and detection

The current state-of-the-art measurements of CIB are provided by the *Planck* satellite at frequencies 216, 353, 545, and 857 GHz. These provide high-fidelity CIB maps within the multipole range of $200 \gtrsim L \gtrsim 2500$. Similar to Ref. [40], however, we also find that the prospects to reconstruct the large-scale radial velocity field from *Planck* CIB maps is not optimistic due to *Planck*’s ~ 5 arc-minute resolution and the residual extragalactic foregrounds which are significant even after ILC cleaning. The picture is much more optimistic, however, for the upcoming CCAT-Prime survey, which will make high-resolution measurements of the CIB at a range of frequency bands including 350, 410, and 850 GHz [39].

We define the CIB instrumental noise term as

$$N_{\ell}^{J_{\nu}} = \Delta_T^2 \exp\left(\frac{\ell(\ell+1)\theta_{\text{FWHM}}^2}{8 \ln 2}\right) + \Delta_R^2 \left(\frac{\ell}{\ell_{\text{knee}}}\right)^{\alpha_{\text{knee}}}, \quad (49)$$

and set $\Delta_R^2 = 1000$ and $\alpha_{\text{knee}} = -3.5$ to match anticipated measurements of CCAT Prime [39]. Our choices for the instrumental noise of the *Planck* and CCAT-prime surveys are shown in Table IV. The anticipated signal and noise spectra matching CCAT-Prime specifications were shown in Fig. 2.

In order to build intuition on the information contained in the reconstructed velocity field, we first perform a principal component analysis (PCA). We calculate a diagonal matrix with entries equal to the signal-to-noise ratio of each principle component via the Karhunen-Loeve technique as

$$\mathbf{C}_{\ell}^{\nu \text{PCA}} = \mathbf{R}_3^{\nu} \mathbf{R}_2^{\nu} \mathbf{R}_1^{\nu} \mathbf{S}_{\ell}^{\nu, T} \mathbf{R}_1^{\nu, T} \mathbf{R}_2^{\nu, T} \mathbf{R}_3^{\nu, T}, \quad (50)$$

which consists of three rotations⁴: (1) \mathbf{R}_1^{ν} diagonalizes the noise covariance matrix N_{ℓ}^{ν} at a given measurement frequency ν and multipole ℓ , (2) \mathbf{R}_2^{ν} sets the transformed noise matrix $N_{\ell}^{\nu'} = \mathbf{R}_1^{\nu} N_{\ell}^{\nu} \mathbf{R}_1^{\nu, T}$ to identity, i.e. $N_{\ell}^{\nu'} = \mathbf{I}$, and (3) \mathbf{R}_3 diagonalizes the matrix $\mathbf{R}_2^{\nu} \mathbf{R}_1^{\nu} \mathbf{S}_{\ell}^{\nu, T} \mathbf{R}_2^{\nu, T}$. Here, all matrices are $N_{\text{bin}} \times N_{\text{bin}}$ square matrices where N_{bin} is the

⁴Note we have omitted the multipole ℓ dependence of the rotation matrices here for brevity.

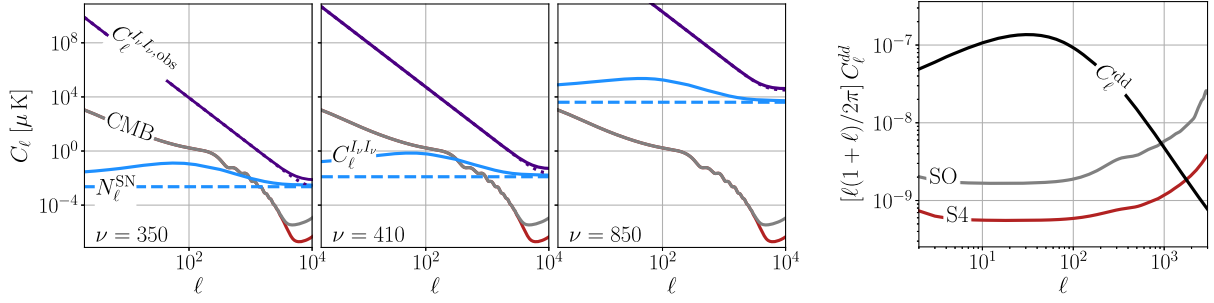


FIG. 2. Left: the anticipated signal and noise spectra as a function of multipoles ℓ for the CCAT-Prime measurements at frequencies $\nu = \{350, 410, 850\}$. The solid blue curves correspond to the anticipated CIB signal, the dashed blue curves correspond to the shot noise, the dotted purple lines correspond to the instrumental noise and the solid purple lines correspond to the total spectra anticipated to be observed. The instrumental noise is anticipated to dominate the observed spectra except at highest multipoles. The solid red and gray curves correspond to the CMB signal including foregrounds and noise anticipated for CMB-S4 (S4) and the Simons Observatory (SO), respectively. Right: the CMB weak-lensing deflection power-spectrum C_ℓ^{dd} shown together with the reconstruction-noise forecasts for CMB-S4 and the SO.

number of redshift bins considered in our analysis, T superscripts indicate matrix transposition and \mathbf{S}_ℓ is the covariance of the radial velocity field signal satisfying $(\mathbf{S}_\ell)_{\alpha\beta} = C_{\ell,\alpha\beta}^{\bar{v}}$. In order to calculate the detection significance, we omit the cosmic variance (\mathbf{S}_ℓ) from the noise covariance, setting $(\mathbf{N}_\ell^\nu)_{\alpha\beta} = N_{\ell,\alpha\beta}^{\bar{v}}$ defined in Eq. (44).

The resulting $\mathbf{C}_\ell^{\nu\text{PCA}}$ is a diagonal matrix whose entries correspond to the (detection) signal-to-noise ratio (SNR) of the N_{bin} principle components for a given velocity mode. We show the detection SNR from the first and second principle components of the velocities anticipated to be reconstructed from the CCAT-Prime survey measurements on the left panel of Fig. 3. The shape of the first principle component in the redshift basis for multipole $\ell = 2$ is shown on the right panel of the same figure. It is valuable to note that the contribution to the lower-frequency CIB signal comes largely from redshifts $2 < z < 4$; the anticipated period of helium reionization.

D. Weak lensing

In order to fully capitalize on the high-redshift probes of large-scale structure, we also consider lensing reconstruction from measurements of CMB temperature and polarization. We calculate the minimum-variance noise on the reconstructed lensing deflection using the standard quadratic estimator from Ref. [51], which we described in Appendix B of Ref. [43]. We take the CMB polarization noise spectra to satisfy $N_\ell^{EE} = N_\ell^{BB} = 2N_\ell^{TT}$, as is expected with fully polarized detectors, and set the maximum multipole used in lensing reconstruction ℓ_{max} equal to 5000 (7000) for reconstructions including the temperature signal (only polarization signals). Our choices for the parameters describing CMB measurement noise are given in Table II. The lensing reconstruction noise and the lensing power spectrum are shown on the right panel of Fig. 2. We use CLASS_DELENS³ code for our calculations which provides a self-consistent, iterative, all-orders treatment of

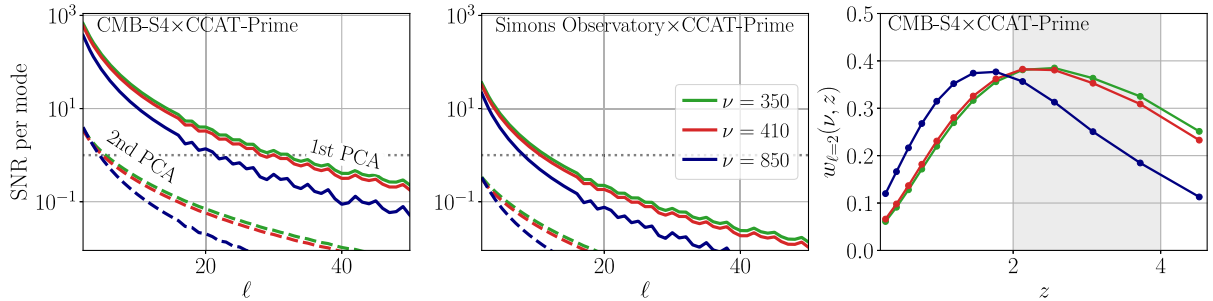


FIG. 3. The left and center panels show the anticipated SNR per mode from the first (second) principle components corresponding to the CCAT-Prime measurements, shown with solid (dashed) lines. In both panels we show results for measurements at frequencies $\nu = \{350, 410, 850\}$ GHz. The left (center) panel corresponds to using anticipated CMB noise levels matching CMB-S4 (Simons Observatory) for kSZ tomography (velocity reconstruction). The right panel shows the redshift weights of the first principle component for $\ell = 2$, normalized to satisfy $\sum_\alpha w_2(\nu, z_\alpha) = 1$ for $\alpha = \{1, \dots, N_{\text{bin}}\}$. Here, we only show the results for correlations of CIB with CMB-S4-like CMB maps; since results from using a SO-like CMB experiment are largely identical. For all panels we set the number of redshift bins N_{bin} equal to 13. Increasing N_{bin} does not improve the results as both the signal and the reconstruction noise are highly correlated between different redshift bins.

CMB delensing and lensing-noise reconstruction on the curved sky, as described in Ref. [43].

V. PROBING HELIUM REIONIZATION

As an application of the high-redshift large-scale-structure probes and velocity reconstruction, here we evaluate the prospects to probe helium reionization with velocity tomography. Similar to Ref. [1], we characterize the change in the ionization fraction during helium reionization with a hyperbolic tangent

$$\bar{x}_e(z) = \frac{1}{2} \left[2 + \Delta\bar{x}_{\text{He}} - \Delta\bar{x}_{\text{He}} \tanh\left(\frac{y(z_{\text{re}}^{\text{He}}) - y(z)}{\Delta_y^{\text{He}}}\right) \right], \quad (51)$$

where $\Delta\bar{x}_{\text{He}}$ determines the total change in the mean ionization fraction during helium reionization, $z_{\text{re}}^{\text{He}}$ is the redshift halfway through the helium reionization, $y(z) = (1+z)^{3/2}$, and Δ_y^{He} parametrizes the duration of the transition. In what follows we will replace $\Delta\bar{x}_{\text{He}}$ with Y_p and the Δ_y^{He} parameter with Δ_z^{He} , which we define as the duration in redshift of the central 50% change in ionization fraction. We use CAMB to calculate $\partial Y_p / \partial \Delta\bar{x}_{\text{He}}$.

The reconstructed velocities depend on the free electron fraction through the optical depth. If helium reionization has not been modeled correctly to match the data, the resulting velocity reconstruction will be biased. We find to a good approximation the reconstructed velocities from kSZ tomography using both galaxies and CIB satisfy $\hat{v}^\alpha(\hat{n}) \simeq [\bar{x}_e(z_\alpha) / \bar{x}_e(z_\alpha)_{\text{fid}}] b_X(z_\alpha) \bar{v}^\alpha(\hat{n})$, where $\bar{x}_e(z) / \bar{x}_e(z)_{\text{fid}}$ is equal to unity if the true helium reionization match the fiducial model, and $b_X(z_\alpha)$ is the standard kSZ optical-depth bias due to mismodeling of the cross power of electron and some tracer of large-scale structure X at small scales, as described in e.g. Refs. [2–4].

In order to measure the information content of the correlated reconstructed velocity and density observables, we define an ensemble information matrix as

$$\mathcal{F}_{ik} = \sum_{\ell=\ell_{\text{min}}}^{\ell_{\text{max}}} f_{\text{sky}} \frac{2\ell+1}{2} \times \text{Tr} \left[\frac{\partial \mathcal{S}_\ell}{\partial \pi_i} (\mathcal{S}_\ell + \mathcal{N}_\ell)^{-1} \frac{\partial \mathcal{S}_\ell}{\partial \pi_k} (\mathcal{S}_\ell + \mathcal{N}_\ell)^{-1} \right], \quad (52)$$

where \mathcal{S}_ℓ (\mathcal{N}_ℓ) is the signal (noise) matrix and $\partial \mathcal{S}_\ell / \partial \pi_i$ represents the derivative of the signal matrix with respect to parameter π_i . Throughout this paper we set f_{sky} equal to 0.4 (0.3) to match forecasts including the anticipated CMB-S4 (Simons Observatory) measurements. Similarly, we assume the joint sky coverages of large-scale structure tracers we consider here (measurements of CCAT-Prime and galaxy surveys) with CMB-S4 and Simons Observatory are 0.4 and 0.3, respectively. We set $\ell_{\text{max}} = 200$ and $\ell_{\text{min}} = 2$ throughout, unless specified otherwise. In addition to the

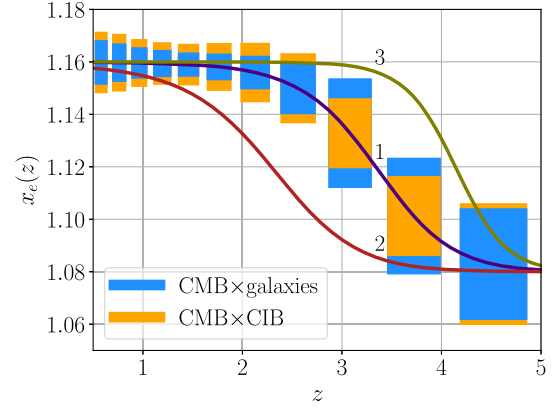


FIG. 4. The 1σ errors on the amplitudes of reconstructed velocity fields from combination of CMB and galaxies (CIB) shown with blue (orange) error bars. In both cases we also include the cross-correlation of the reconstructed large-scale velocity with the galaxy density, latter anticipated to match LSST observations. The coloured solid lines labeled 1 to 3 correspond to three distinct helium reionization models with varying fiducial values and considerations described in the text.

parameters characterizing helium reionization, we consider bias parameters for the galaxy, velocity and lensing observables, as well as the amplitude of primordial scalar perturbations A_s as free parameters in our forecasts.

We demonstrate the measurement accuracy of the velocity reconstruction from kSZ tomography using galaxies (blue error bars) and CIB (orange error bars) in Fig. 4. The error bars in this figure correspond to 1σ errors on the amplitudes of the reconstructed velocity fields in 13 redshift bins, which we define as $\hat{v}_{\ell m}^\alpha = b_\alpha \bar{v}_{\ell m}^\alpha$. Here, the information matrix consists of (1) the covariance of velocity fields reconstructed at each redshift bin, $C_{\ell, \alpha\beta}^{\hat{v}} = C_{\ell, \alpha\beta}^{\bar{v}} + N_{\alpha\beta\ell}^{\bar{v}}$, where $N_{\alpha\beta\ell}^{\bar{v}}$ is the reconstruction noise defined in Eq. (45) for CMB \times CIB tomography and in Eq. (24) for CMB \times galaxy tomography and $C_{\ell, \alpha\beta}^{\bar{v}}$ is the redshift-binned radial velocity power spectra; (2) the cross-correlation between the reconstructed velocity and galaxy fields, $C_{\ell, \alpha\beta}^{\bar{v}\delta_g}$; as well as (3) the covariance of the observed large-scale galaxy fields $C_{\ell, \alpha\beta}^{\delta_g\delta_g, \text{obs}}$, which includes the galaxy shot noise.

For kSZ tomography using CIB, we consider three frequencies at $\{350, 410, 850\}$ GHz and experimental specifications matching CCAT-Prime. The information matrix in this case has the shape $(4N_{\text{bin}} \times 4N_{\text{bin}})$ and includes the cross-correlation between reconstructed velocities at different frequencies and redshifts. For kSZ tomography using galaxies, the information matrix has the shape $(2N_{\text{bin}} \times 2N_{\text{bin}})$. In both cases we forecast assuming CMB-S4 and LSST. In addition to the velocity bias parameters we defined above, here we also marginalize over the galaxy biases and the three reionization parameters.

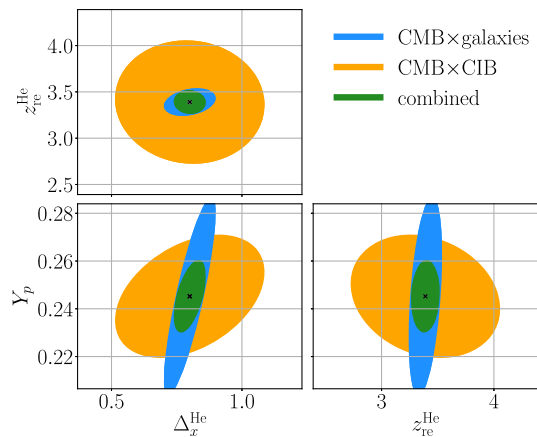


FIG. 5. The 1σ error contours on helium reionization model parameters defined in the text. Similar to Fig. 4, blue (orange) contours correspond to reconstructed velocity fields from combination of CMB and galaxies (CIB).

The solid lines labeled with numbers 1 to 3 correspond to three helium reionization models with fiducial choices for $(z_{\text{re}}^{\text{He}}, \Delta_x^{\text{He}})$ set equal to $(3.34, 0.8)$, $(2.29, 0.79)$, and $(4.14, 0.58)$, respectively. We take $Y_p = 0.245$ ($\Delta x_{\text{He}} \simeq 0.08$) for all models. As done in Ref. [1], these models are chosen to roughly match models H1, H3 and H6, considered in Ref. [52], respectively, which represent several plausible and distinct models of helium reionization.⁵ Distinguishing between these models can provide an independent determination of the average luminosity and abundance of quasars and their interactions with the IGM, which complements direct measurements from spectroscopic surveys.

Next, we forecast the measurement accuracy of helium reionization model parameters assuming model 1 in Fig. 5. Similar Fig. 4, we consider a joint analysis of small-scale CMB measurements matching the anticipated noise and foregrounds of the upcoming CMB-S4 survey; galaxy surveys with specifications matching the upcoming LSST survey; and CIB measurements that are anticipated to match the upcoming CCAT-Prime survey. The blue (orange) contours correspond to 1σ measurement errors on helium reionization parameters from measurements of the galaxy and velocity fields on large scales, latter reconstructed from combination of CMB and galaxies (CIB) on small scales. The green contours correspond to the combined measurement accuracy anticipated from these observables.

⁵Model H1 reproduces the quasar spectrum measured by Ref. [53], the quasar abundance measured by Refs. [19–21], and quasar clustering measured by BOSS [54]. Model H3 considers a quasar abundance that is reduced by a factor of 2. This model is consistent with the measured uncertainties but yields a slightly delayed reionization scenario. Model H6 reproduces the seminumeric models of Ref. [55] and uses a uniform UV background rather than explicit quasar sources.

For the results in Fig 5, we have defined a parametrized velocity bias in the form $b^X(z) = b_0^X + b_1^X z + b_2^X z^2$, where $X = \{\text{CIB, gal}\}$, separately for the velocity reconstructions using CIB and galaxies. We set the fiducial values of $\{b_0^{\text{CIB}}, b_1^{\text{CIB}}, b_2^{\text{CIB}}\}$ to $\{0.84, 0.74, 0.32\}$ following Refs. [41,56]. For the kSZ optical depth bias from kSZ using galaxies, we set the fiducial value b_0^{gal} to unity and $\{b_1^{\text{gal}}, b_2^{\text{gal}}\}$ to zero. We also define the bias on the large-scale galaxy density with the same parametrization. When inferring errors on helium reionization model parameters, we marginalize over these biases as well as the amplitude of scalar primordial fluctuations A_s . Unless otherwise specified, we also assume 10% priors on the bias parameters b_0^{CIB} and b_0^{gal} , latter can be potentially achieved by measurements of the CMB polarization (e.g. [57,58]), the moving lens effect [59–61] or the fast radio bursts [62]. Our results for kSZ tomography using LSST galaxies match our earlier work [1] within a factor of ~ 2 , although note Ref. [1] used a three-dimensional box formalism. For the experimental specifications matching CCAT-Prime and LSST, we find kSZ tomography with these tracers provide comparable information on the helium reionization.

In order to assess the detection prospects of helium reionization, we consider the SNR on $\Delta \bar{x}_e$ after marginalizing over other reionization and bias parameters. For velocity reconstruction using CIB, we consider the CCAT-Prime specifications throughout. We find that the combination of reconstructed velocities from the Simons Observatory and CIB or DESI galaxies will likely not reach sufficient SNR to detect helium reionization when considered in isolation. Nevertheless, we find that hints of helium reionization may be detected at $\sim 1\text{--}2\sigma$ from the joint analysis of these signals and weak lensing. For CMB-S4 and an LSST-like survey assuming specifications matching the “gold sample,” we find helium reionization may be detected at around $\sim 2\text{--}4\sigma$ from CIB- and galaxy-reconstructed velocity fields in isolation; and that the detection SNR can reach $\sim 6\text{--}8\sigma$ if these signals are jointly analyzed. We show the detection SNR of helium reionization from different considerations in Table V. Including anticipated high-redshift galaxy dropouts following Refs. [63–65] increase the prospects of detecting helium reionization with LSST by over $\sim 30\text{--}40$ percent using the methods we consider here.

The prospect of measuring cosmological signatures at high redshifts using kSZ tomography depends significantly on the lowest accessible multipoles (largest angular scales) at which the velocity fields can be reconstructed. In Fig. 6 we demonstrate the dependence of the helium reionization detection as well as the figure of merit (FOM) on the minimum multipole we consider in our forecasts ℓ_{min} . The FOM provides a simple quantitative summary of how well a given observable can improve the prospects of measuring cosmological signatures at high-redshifts, and is defined as

TABLE V. Detection SNR of helium reionization defined as the 1σ measurement error on the $\Delta\bar{x}_{\text{He}}$ parameter after marginalizing over other reionization parameters and biases as defined in the text. Here, $\hat{v}_{\text{CIB}}^\alpha$ refers to the radial velocity field reconstructed from small-scale CMB \times CIB cross-correlation. We use CIB measurements with anticipated experimental specifications matching CCAT-Prime throughout. The velocity fields reconstructed from cross-correlation of CMB and galaxies are shown with $\hat{v}_{\text{gal}}^\alpha$. Here, δ_g^α refers to the large-scale galaxy field anticipated to be observed with either DESI or LSST gold sample (GS). The lensing potential reconstructed from CMB temperature and polarization fluctuations is shown with $\hat{\phi}$.

Observables	Experiments	
	SO & DESI	CMB-S4 & LSST (GS)
$\hat{v}_{\text{CIB}}^\alpha, \delta_g^\alpha$	0.8	3.9
$\hat{v}_{\text{gal}}^\alpha, \delta_g^\alpha$	0.5	2.8
$\hat{v}_{\text{CIB}}^\alpha, \hat{v}_{\text{gal}}^\alpha, \delta_g^\alpha$	1.2	6.5
$\hat{v}_{\text{CIB}}^\alpha, \hat{v}_{\text{gal}}^\alpha, \delta_g^\alpha, \hat{\phi}$	1.6	6.9

FOM = $\sqrt{\det \mathcal{F}_{ij}^{-1}}$ where \mathcal{F}_{ij}^{-1} is the information matrix defined in Eq. (52). We find the FOM improves by a factor of ~ 5 for the reconstructed velocities using CIB and

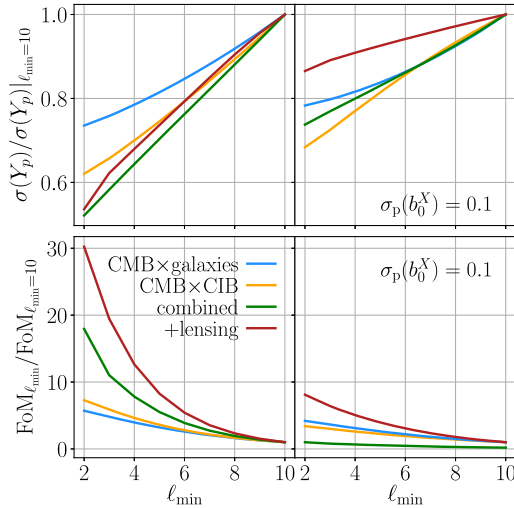


FIG. 6. Sensitivity of the statistical power of kSZ tomography to largest scales considered in the analysis. Upper panels show the sensitivity of measurement of the primordial helium abundance Y_p , parametrized as the ratio between the error on Y_p for a choice of ℓ_{\min} and when ℓ_{\min} is set to 10. The lower panels correspond to fractional improvement in the FOM as a function of ℓ_{\min} . The right panels correspond to assuming 10 percent priors on the velocity bias parameters. The solid blue lines correspond to kSZ tomography using LSST galaxies as described in the text. The orange lines correspond to kSZ tomography using CIB. Green lines correspond to combination of these observables. The red lines also include the reconstructed lensing potential from measurement of CMB weak lensing.

galaxies in isolation, and by a factor ~ 15 when these observables are jointly analyzed. We find the improvement of the FOM is more enhanced when lensing reconstruction is also considered in the analysis. These results are shown on the lower panels of Fig. 6. The lower-right panel corresponds to assuming no priors on the reconstructed velocity, while the lower-left panel assumes 10 percent priors satisfying $\sigma_p(b_0^X) = 0.1$ where $X = \{\text{CIB, gal}\}$. The reduced sensitivity of the statistical power of observables when we consider priors on these biases suggests a significant portion of the statistical power on large scales contribute to constraining these parameters.

The upper panels on Fig. 6 correspond to fractional improvement on the errors on Y_p compared to assuming $\ell_{\min} = 10$. The increase in error from increasing ℓ_{\min} can be seen to reach a factor ~ 2 by $\ell_{\min} \sim 6$ if no priors are assumed on the velocity reconstruction. Similar to the FOM, assuming 10% priors on these parameters lowers the sensitivity of the measurement accuracy to ℓ_{\min} . Overall, we note that our ability to reconstruct largest angles will play a crucial role in realizing the prospects of cosmological inference at high redshifts including detecting and characterizing helium reionization using kSZ tomography.

VI. DISCUSSION

Our results suggest detecting and characterizing helium reionization in the next 1–3 years via kSZ tomography using upcoming surveys such as the Simons Observatory and DESI may be difficult. However we note that the forecasts we included involving DESI are likely somewhat pessimistic given the choice of the low number of redshift bins we considered for this experiment. As the photometric redshift errors will be very small for DESI, we would expect increasing the number of redshift bins would increase the information content of the reconstructed velocities and galaxy-velocity cross-correlation for kSZ tomography using DESI galaxies in principle. Moreover, futuristic experiments such as the proposed MegaMapper [66,67] and CMB-HD [68] are likely to improve the prospects of probing helium reionization dramatically as suggested in Ref. [1].

Furthermore, the reionization of helium may potentially effect the selection functions of the high-redshift quasars and galaxies, as well as the star formation rate inferred from the CIB signal as the ionizing processes can modulate the ultraviolet background fluctuations and the absorption lines used for inferring redshifts with spectroscopic imaging surveys such as DESI and MegaMapper. Going forward, these effects should be accounted for and modeled for an unambiguous characterization and detection of the helium reionization and can both act as increasing the high-redshift observables' sensitivity to helium reionization as well as potentially introducing biases or confusion.

The joint analysis of tracers of large-scale velocity fluctuations reconstructed from small-scale CMB and

different LSS observables, large-scale density fluctuations from galaxy distributions, and reconstructed lensing potential may prove more challenging in practice than what we have considered here, as spurious correlations between these observables may arise in the case the same data (such as the same CMB maps) are used throughout. Also going forward, the prospects of jointly analyzing early structure formation with the methods highlighted here could be tested with realistic simulations including non-Gaussian foregrounds and systematics, and astrophysical properties including the choices made for the halo model of galaxies and electrons in this work could be taken into account consistently via a forward-modeling framework, for example. In what follows, we could make these advances to better identify the true prospects of characterizing these epochs with cross-correlation studies.

Finally, another difficulty posed by probing the epoch of helium reionization with the technique discussed here is that the mean electron fraction should also vary with the fraction of baryons that is locked up in astrophysical objects such as stars, stellar remnants (including baryons that have disappeared into black holes), molecular and atomic clouds, and any ionized systems that are optically thick to Thomson scattering. Such effects are not taken into account in our modeling of the ionized fraction and may not be distinguished from measurements using SZ effects alone. The expected variations in the fraction of baryons

turned to stars are of a few percent, comparable to the abundance of helium by number, and the measurement of the mean electron fraction of the Universe is a combination of multitude of factors including reionization of hydrogen and helium, plus the fractional reservoirs of baryons in the HI damped Ly α absorption systems and stars, which are Thomson-thick repositories for ionized matter, constituting to a significant portion of baryons, and should be modeled together with helium reionization.

Nevertheless, our results are promising and should motivate further analysis of the prospects of cross-correlation science in the near future with ongoing stage-3 and upcoming stage-4 cosmology experiments. The epoch of helium reionization in particular carries valuable and novel information about astrophysics and cosmology that can potentially be accessed in the foreseeable future. In a series of upcoming works we will continue to explore the reach of this program, extending the observables and techniques introduced here.

ACKNOWLEDGMENTS

We thank Fiona McCarthy, Matthew Johnson and Simone Ferraro for useful conversations. We thank Fiona McCarthy for her contributions to the conceptualization of this project. S.C.H. was supported by the Horizon Fellowship from Johns Hopkins University.

-
- [1] S. C. Hotinli, S. Ferraro, G. P. Holder, M. C. Johnson, M. Kamionkowski, and P. La Plante, *Phys. Rev. D* **107**, 103517 (2023).
 - [2] A.-S. Deutsch, E. Dimastrogiovanni, M. C. Johnson, M. Münchmeyer, and A. Terrana, *Phys. Rev. D* **98**, 123501 (2018).
 - [3] K. M. Smith, M. S. Madhavacheril, M. Münchmeyer, S. Ferraro, U. Giri, and M. C. Johnson, *arXiv:1810.13423*.
 - [4] M. Münchmeyer, M. S. Madhavacheril, S. Ferraro, M. C. Johnson, and K. M. Smith, *Phys. Rev. D* **100**, 083508 (2019).
 - [5] P. Zhang and M. C. Johnson, *J. Cosmol. Astropart. Phys.* **06** (2015) 046.
 - [6] S. C. Hotinli, J. B. Mertens, M. C. Johnson, and M. Kamionkowski, *Phys. Rev. D* **100**, 103528 (2019).
 - [7] J. I. Cayuso and M. C. Johnson, *Phys. Rev. D* **101**, 123508 (2020).
 - [8] M. A. Alvarez, S. Ferraro, J. C. Hill, R. Hložek, and M. Ikape, *Phys. Rev. D* **103**, 063518 (2021).
 - [9] S. Ferraro and K. M. Smith, *Phys. Rev. D* **98**, 123519 (2018).
 - [10] K. M. Smith and S. Ferraro, *Phys. Rev. Lett.* **119**, 021301 (2017).
 - [11] S. C. Hotinli and M. C. Johnson, *Phys. Rev. D* **105**, 063522 (2022).
 - [12] N. Anil Kumar, G. Sato-Polito, M. Kamionkowski, and S. C. Hotinli, *Phys. Rev. D* **106**, 063533 (2022).
 - [13] N. A. Kumar, S. C. Hotinli, and M. Kamionkowski, *Phys. Rev. D* **107**, 043504 (2023).
 - [14] S. Foreman, S. C. Hotinli, M. S. Madhavacheril, A. van Engelen, and C. D. Kreisch, *Phys. Rev. D* **107**, 083502 (2023).
 - [15] Ž. Ivezić *et al.* (LSST Collaboration), *Astrophys. J.* **873**, 111 (2019).
 - [16] K. N. Abazajian *et al.* (CMB-S4 Collaboration), *arXiv:1610.02743*.
 - [17] K. Abazajian *et al.* (CMB-S4 Collaboration), *Astrophys. J.* **926**, 54 (2022).
 - [18] Y. Shen and L. C. Ho, *Nature (London)* **513**, 210 (2014).
 - [19] N. P. Ross, I. D. McGreer, M. White, G. T. Richards, A. D. Myers, N. Palanque-Delabrouille, M. A. Strauss, S. F. Anderson, Y. Shen, W. N. Brandt, C. Yèche, M. E. C. Swanson *et al.*, *Astrophys. J.* **773**, 14 (2013).
 - [20] D. Masters, P. Capak, M. Salvato, F. Civano, B. Mobasher, B. Siana, G. Hasinger, C. D. Impey, T. Nagao, J. R. Trump, H. Ikeda, M. Elvis, and N. Scoville, *Astrophys. J.* **755**, 169 (2012).
 - [21] I. D. McGreer, L. Jiang, X. Fan, G. T. Richards, M. A. Strauss, N. P. Ross, M. White, Y. Shen, D. P. Schneider,

- A. D. Myers, W. N. Brandt, C. DeGraf, E. Glikman, J. Ge, and A. Streblyanska, *Astrophys. J.* **768**, 105 (2013).
- [22] I. D. McGreer, X. Fan, L. Jiang, and Z. Cai, *Astron. J.* **155**, 131 (2018).
- [23] Z. Pan, L. Jiang, X. Fan, J. Wu, and J. Yang, *Astrophys. J.* **928**, 172 (2022).
- [24] P. F. Hopkins, A. Lidz, L. Hernquist, A. L. Coil, A. D. Myers, T. J. Cox, and D. N. Spergel, *Astrophys. J.* **662**, 110 (2007).
- [25] T. M. Schmidt, G. Worseck, J. F. Hennawi, J. X. Prochaska, and N. H. M. Crighton, *Astrophys. J.* **847**, 81 (2017).
- [26] K. Inayoshi, E. Visbal, and Z. Haiman, *Annu. Rev. Astron. Astrophys.* **58**, 27 (2020).
- [27] C. Pitrou, A. Coc, J.-P. Uzan, and E. Vangioni, *Phys. Rep.* **754**, 1 (2018).
- [28] Z. Hou, R. Keisler, L. Knox, M. Millea, and C. Reichardt, *Phys. Rev. D* **87**, 083008 (2013).
- [29] G. D. Becker, J. S. Bolton, M. G. Haehnelt, and W. L. W. Sargent, *Mon. Not. R. Astron. Soc.* **410**, 1096 (2011).
- [30] E. Boera, M. T. Murphy, G. D. Becker, and J. S. Bolton, *Mon. Not. R. Astron. Soc.* **441**, 1916 (2014).
- [31] K. N. Telikova, P. S. Shternin, and S. A. Balashev, *Astrophys. J.* **887**, 205 (2019).
- [32] D. Syphers, S. F. Anderson, W. Zheng, A. Meiksin, D. P. Schneider, and D. G. York, *Astron. J.* **143**, 100 (2012).
- [33] J. I. Cayuso, M. C. Johnson, and J. B. Mertens, *Phys. Rev. D* **98**, 063502 (2018).
- [34] N. Aghanim, M. Ashdown, J. Aumont, C. Baccigalupi, M. Ballardini, A. Banday, R. Barreiro, N. Bartolo, S. Basak, K. Benabed *et al.*, *Astron. Astrophys.* **596**, A109 (2016).
- [35] D. S. Y. Mak, A. Challinor, G. Efstathiou, G. Lagache, and G. Lagache, *Mon. Not. R. Astron. Soc.* **466**, 286 (2017).
- [36] B. Yu, J. C. Hill, and B. D. Sherwin, *Phys. Rev. D* **96**, 123511 (2017).
- [37] D. Lenz, O. Doré, and G. Lagache, *Astrophys. J.* **883**, 75 (2019).
- [38] F. McCarthy, M. S. Madhavacheril, and A. S. Maniyar, *arXiv:2210.01049*.
- [39] M. Aravena *et al.* (CCAT-Prime Collaboration), *Astrophys. J. Suppl. Ser.* **264**, 7 (2023).
- [40] F. McCarthy and M. C. Johnson, *Phys. Rev. D* **102**, 043520 (2020).
- [41] F. McCarthy and M. S. Madhavacheril, *Phys. Rev. D* **103**, 103515 (2021).
- [42] J. Cayuso, R. Bloch, S. C. Hotinli, M. C. Johnson, and F. McCarthy, *J. Cosmol. Astropart. Phys.* **02** (2023) 051.
- [43] S. C. Hotinli, J. Meyers, C. Trendafilova, D. Green, and A. van Engelen, *J. Cosmol. Astropart. Phys.* **04** (2022) 020.
- [44] N. Battaglia, *J. Cosmol. Astropart. Phys.* **08** (2016) 058.
- [45] M. S. Madhavacheril, N. Battaglia, and H. Miyatake, *Phys. Rev. D* **96**, 103525 (2017).
- [46] H. Park, P. R. Shapiro, E. Komatsu, I. T. Iliev, K. Ahn, and G. Mellema, *Astrophys. J.* **769**, 93 (2013).
- [47] G. Lagache, M. Béthermin, L. Montier, P. Serra, and M. Tucci, *Astron. Astrophys.* **642**, A232 (2020).
- [48] A. Lewis, A. Challinor, and A. Lasenby, *Astrophys. J.* **538**, 473 (2000).
- [49] DESI Collaboration, *arXiv:1611.00036*.
- [50] P. A. Abell *et al.* (LSST Science Collaboration), *arXiv:0912.0201*.
- [51] T. Okamoto and W. Hu, *Phys. Rev. D* **67**, 083002 (2003).
- [52] P. La Plante, H. Trac, R. Croft, and R. Cen, *Astrophys. J.* **841**, 87 (2017).
- [53] E. Lusso, G. Worseck, J. F. Hennawi, J. X. Prochaska, C. Vignali, J. Stern, and J. M. O'Meara, *Mon. Not. R. Astron. Soc.* **449**, 4204 (2015).
- [54] M. White *et al.*, *Mon. Not. R. Astron. Soc.* **424**, 933 (2012).
- [55] F. Haardt and P. Madau, *Astrophys. J.* **746**, 125 (2012).
- [56] A. S. Maniyar, M. Béthermin, and G. Lagache, *Astron. Astrophys.* **614**, A39 (2018).
- [57] N. Lee, S. C. Hotinli, and M. Kamionkowski, *Phys. Rev. D* **106**, 083518 (2022).
- [58] S. C. Hotinli, G. P. Holder, M. C. Johnson, and M. Kamionkowski, *J. Cosmol. Astropart. Phys.* **10** (2022) 026.
- [59] S. C. Hotinli, K. M. Smith, M. S. Madhavacheril, and M. Kamionkowski, *Phys. Rev. D* **104**, 083529 (2021).
- [60] S. C. Hotinli, M. C. Johnson, and J. Meyers, *Phys. Rev. D* **103**, 043536 (2021).
- [61] S. C. Hotinli, J. Meyers, N. Dalal, A. H. Jaffe, M. C. Johnson, J. B. Mertens, M. Münchmeyer, K. M. Smith, and A. van Engelen, *Phys. Rev. Lett.* **123**, 061301 (2019).
- [62] M. S. Madhavacheril, N. Battaglia, K. M. Smith, and J. L. Sievers, *Phys. Rev. D* **100**, 103532 (2019).
- [63] S. Ferraro, E. Schaan, and E. Pierpaoli, *arXiv:2205.10332*.
- [64] Y. Ono *et al.*, *Publ. Astron. Soc. Jpn.* **70**, S10 (2018).
- [65] Y. Harikane *et al.*, *Publ. Astron. Soc. Jpn.* **70**, S11 (2018).
- [66] D. J. Schlegel *et al.*, *Bull. Am. Astron. Soc.* **51**, 229 (2019).
- [67] S. Ferraro, N. Sailer, A. Slosar, and M. White, *arXiv:2203.07506*.
- [68] S. Aiola *et al.* (CMB-HD Collaboration), *arXiv:2203.05728*.